Revised version submitted to SuperAlloys 2020. Different from the finally published version. May contain formatting, typographical and other errors.

Local mechanical properties at the dendrite scale of Ni-base superalloys studied by advanced high temperature indentation creep and micropillar compression tests

L. Haußmann[a,*], S. Neumeier[a], M. Kolb[a], J. Ast[b,c], G. Mohanty[b,d], J. Michler[b], M. Göken[a]

[a] Friedrich-Alexander-Universität Erlangen-Nürnberg, Department of Materials Science & Engineering, Institute I: General Materials Properties, Martensstr.5, 91058, Erlangen, Germany
[b] Empa, Swiss Federal Laboratories for Materials Science and Technology, Laboratory for Mechanics of Materials and Nanostructures, Feuerwerkerstraße 39, CH-3602 Thun, Switzerland
[c] Fraunhofer-Institut für Keramische Technologien und Systeme IKTS, Korrelative Mikroskopie und Materialdaten, Äußere Nürnberger Strasse 62, 91301 Forchheim, Germany
[d] Tampere University, Materials Science and Environmental Engineering, 33014 Tampere, Finland

*Corresponding author. E-Mail address: lukas.haussmann@fau.de (Lukas Haußmann)

Abstract

Chemical inhomogenities due to dendritic solidification of Ni base superalloys result in different local microstructures with varying mechanical properties. New indentation creep test methods allow probing of the local creep properties at the dendrite scale at high temperatures. The as-cast single crystalline Ni-base superalloy ERBO1A (a derivative alloy of CMSX-4) was investigated and electron-probe microanalysis (EPMA) measurements revealed strong segregation of e.g. Re and W in the dendritic region and e.g. Ta in the interdendritic region. Indentation creep experiments at 750 °C and micropillar compression tests at 785 °C were conducted in both regions and a higher creep strength was found in the dendritic region compared to the interdendritic region. Theoretical models for solid solution hardening as well as γ′ precipitation hardening confirm these results, since they predict a higher strength in the dendritic region than in the interdendritic region. Compared with the fully heat treated state, a smaller difference in the local mechanical properties or even a reverse strength ratio of the dendritic and interdendritic region can be expected.

Keywords: Ni-base Superalloy; Indentation Creep; Micropillar Compression; Dendritic Segregations;

1. Introduction

Microstructural inhomogeneities and concentration gradients are present in nearly all metallic alloys. In Ni- and Co-based superalloys, the dendritic microstructure, diffusion zones between substrate and coatings, γ′ precipitates and other intermetallic phases character determine the macroscopic mechanical properties. Nanomechanical testing methods are very well suited to determine local differences of the mechanical properties [1–3]. Especially, indentation creep testing is a well-suited technique for such investigations, since it allows an examination of the local creep properties at elevated temperatures. Chu and Li [4] introduced already in 1977 an indentation creep method with a cylindrical flat punch indenter. Commonly used pyramidal indenter tips degrade during indentation creep experiments, with a significant influence on the results [5, 6]. However, until today such indentation creep experiments using cylindrical indenters were usually carried out with relatively large indenter tips of diameters ≥ 1 mm [7–9]. Cylindrical flat punch indenters were also used for special applications like characterization of thin films with very small indenter tips of diameters ≤ 1 µm [10, 11] or at low temperatures

[4, 12]. Pyramidal indenters have been used quite intensively to study the individual properties of γ, γ′ and TCP phases [1–3, 13]. However, these pyramidal sharp indenter tips suffer from many limitations when used to study high temperature properties, particularly during long-term indentation creep tests. A crucial factor for nanomechanical high temperature creep experiments is the thermal drift rate. Most nanomechanical methods show relatively high thermal drift rates at high temperatures in the range of nm/s which makes them unsuitable for long-term high temperature experiments. A suitable new testing method was recently introduced by Matschkal-Amberger et al. [14] using a thermomechanical analyzer with a focused ion beam (FIB) milled cylindrical flat punch indenter with a diameter of 20 µm for indentation creep experiments which only leads to thermal drift rates in the range of nm/h.

In this study this new indentation creep method was used together with micropillar compression tests to investigate the influence of segregations at the dendritic and interdendritic regions on the local mechanical properties of the single crystalline Ni-base superalloy ERBO1, which is a derivative alloy of CMSX-4.

2. Experimental Procedures

The nominal composition of Ni-base superalloy ERBO1 is given in Table 1. The material was cast by *Doncasters Castings GmbH* using the Bridgman process as single crystalline plates in [001] orientation. All investigations were performed on as-cast samples. In the following, the as-cast condition is referred to as ERBO1A, whereas the fully heat treated condition is referred to as ERBO1C. Further information on the material can be found in [15].

After standard metallographic sample preparation procedure, the microstructure was characterised using a scanning electron microscope (SEM) *(Crossbeam 1540 EsB, Zeiss)* and the chemical composition was probed by energy dispersive X-ray spectroscopy (EDS) *(Inca Energy 350, Oxford Instruments)*. The chemical analysis on the dendrite scale was determined by electron-probe microanalysis (EPMA) *(JXA-8100, Jeol)* operating at a voltage of 20 kV, spot size of 5 µm and a dwell time of 5 ms. The analysing crystals used for detecting the elements were LiF (Co,W,Ta), TAP (Al,Ni,Hf), PETJ (Ti,Cr) and LIFH (Mo,Re).

Table 1: Nominal composition of ERBO1 in at. %.

	Concentration / at. %									
	Ni	Co	Al	W	Ti	Ta	Cr	Re	Mo	Hf
ERBO1	Bal.	9.8	12.4	2.1	1.3	2.2	7.5	1.0	0.4	0.03

Freestanding micropillars were prepared after the widely used top-down methodology [16] using focused ion beam milling (FIB) *(Crossbeam 540, Zeiss)* in dendritic (DR) and interdendritic (IR) regions of the ERBO1A alloy. All micropillars were milled to a diameter of 4 µm and a height of 12 µm using concentric annular milling patterns with decreasing current and diameter. The starting current for rough milling was 30°kv/15nA which was gradually decreased to a fine milling current of 30 kV / 100 pA. Micropillar compression testing was carried out at 785 °C using a high temperature nanoindenter *(Alemnis AG)*, equipped with a tungsten carbide flat punch indenter (6 µm diameter). Prior to the experiments, the contact drift was minimized by adjusting the sample and tip temperature independently using thermal drift minimization protocols outlined in [17, 18]. The tests were performed in constant displacement control mode with an imposed displacement rate of 10 nm/s. To calculate the flow stress, the diameter measured at the top region of the pillar was used, as indicated in Figure 1(a).

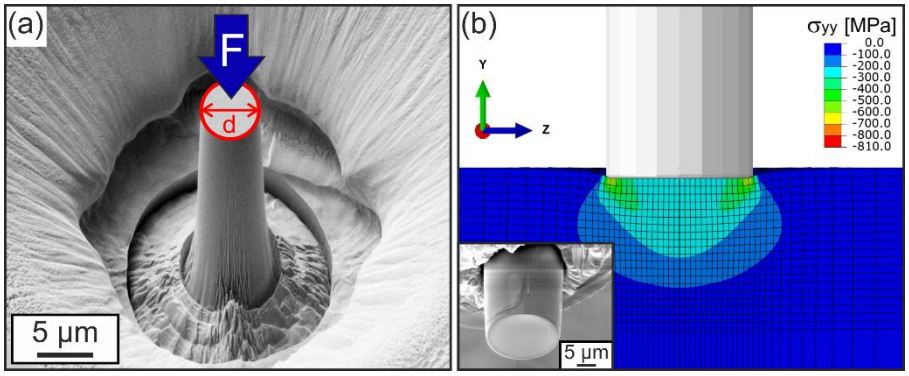

Figure 1: (a) Freestanding micropillar of Ni-base superalloy ERBO1 with diameter d and force F prior to mechanical testing. (b) FE simulation of indentation with a cylindrical flat punch indenter and (inset) FIB milled sapphire indenter tip for indentation creep experiments.

A modified Thermo-Mechanical Analyzer (TMA) *(402 F3 Hyperion, Netzsch)* was used to perform indentation creep experiments under Argon atmosphere at 750 °C and at stress levels of 800 MPa and 1350 MPa. A cylindrical, constant cross-section flat punch indenter (20 µm diameter), FIB milled *(Helios Nanolab 600I, FEI)* from a conical sapphire indenter (*SYNTON-MPD AG)* with an individual manufactured shaft was used to ensure constant stress with increasing indentation depth (see inset Figure 1(b)). This indenter geometry allows a conversion of the indentation creep data into equivalent uniaxial data for σ and $\dot{\varepsilon}$ with the method reported by Matschkal-Amberger et al. [14] as indicated by the FE Simulation in Figure 1(b). For the calculations, conversion factors $C_1 = 0.5$ and $C_2 = 0.564$ [14] were used, which were calculated by crystal plasticity finite element modeling (FEM) simulations for pure Ni at 650°C. To achieve a thermal equilibrium and to reduce the thermal drift, the temperature of the sample and the low force was held constant for 2.5 h prior testing. To avoid oxidation of the samples, all tests were performed under Argon atmosphere. In addition, a Ti foil as oxygen getter was placed close to the sample. The validation of the method is given in [14]. In addition to the creep tests, the microstructure was analyzed close to the indentation sites by FIB cross sections and EDS analysis to determine the γ' volume fraction and precipitate size.

3. Results and Discussion

3.1 Microstructure and segregation behavior

In the BSE images of the microstructure of ERBO1A in Figure 2(a) a brighter contrast reveals an accumulation of heavy elements, such as W or Re, in the DR.

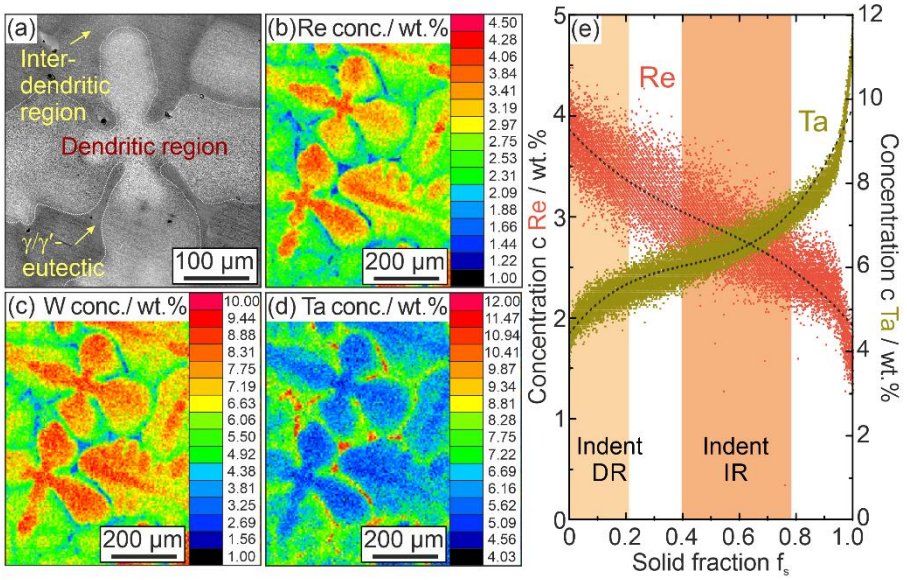

Figure 2: Microstructure of ERBO1A, (a) SEM micrograph of a dendrite in the BSE contrast, and concentration on the dendrite scale of (b) Re, (c) W and (d) Ta determined by EPMA. Re and W segregate to the dendrite core, whereas Ta segregates strongly to the interdendritic region. (e) Shows the concentrations of Re and Ta in dependence of the solid fraction f_s. The regions of the indents in the DR and IR shown in Figure 3 are also marked in (c).

The elemental distribution was analyzed in detail by the EPMA-maps. They demonstrate that Re and W segregate in the dendrite cores (DC) and arms, whereas Ta segregates in the IR, see Figure 2(b)-(d). SEM investigations revealed that the different element concentrations lead to a varying γ′ volume fraction, from 54.8 % in the dendrite core to 66.0 % in the IR close the γ/γ′ eutectic. Parsa et al. have reported a γ′ volume fraction of 72 % in the dendrite core and 77 % in the IR on the same alloy in the fully heat treated condition [15].

In order to assign particular concentrations to the dendritic microstructure, a special sorting algorithm is used to analyze the EPMA data. By sorting the concentration values of each element of the EPMA map it can be estimated when a particular position solidified. This method was already proposed in the literature and used to investigate segregations in Ni- and Co-base superalloys [19–21]. The data points for Re and Ta concentrations from Figure 2(b) and (d) are assigned to the concentration difference of Ta and Re (c_{Ta}-c_{Re}), as this value increases constantly until the end of the solidification. A solid fraction f_s between 0 and 1 is then assigned to the sorted concentrations and the indents placed in the IR and DC (see next section) can be linked with the prevailing chemical concentrations, see Figure 2(e).

3.2 Local mechanical properties

In Figure 3, some of the residual indents after the indentation creep experiments performed at 800 MPa and 750 °C are shown. Figure 3(a) and (c) illustrate an indent in the DR, whereas Figure 3(b) and (d) display an indent positioned in the IR at different magnifications.

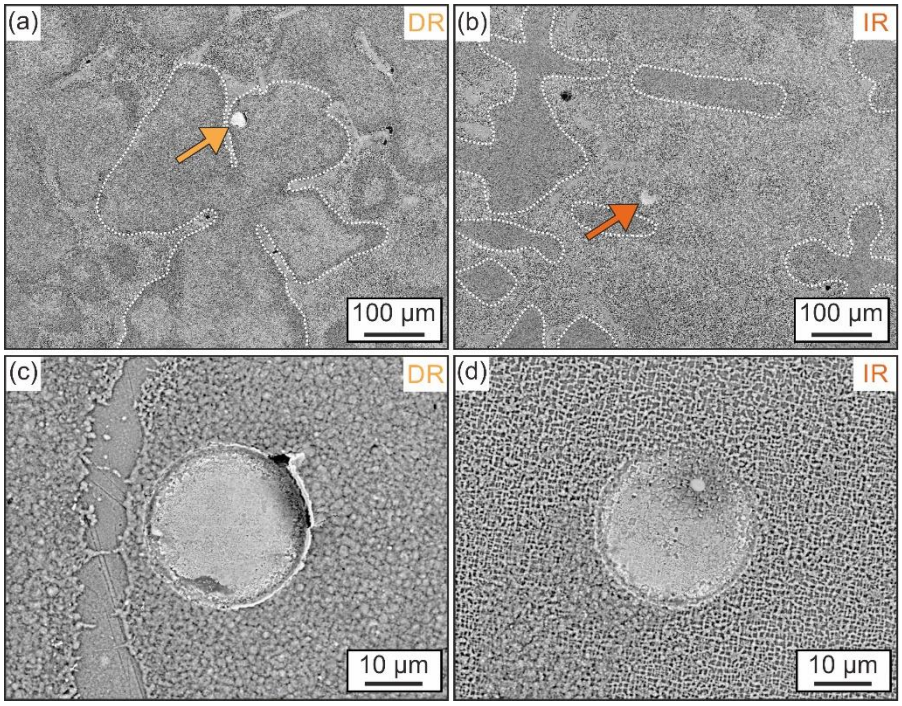

Figure 3: Residual indents after loading with 800 MPa at 750 °C (a) in the dendritic region (DR) and (b) in the interdendritic region (IR) of the alloy ERBO1A. Higher magnifications of the indents are shown in (c) and (d).

The resulting data of the indentation creep experiments, conducted at 800 MPa and 1350 MPa at 750 °C is plotted in Figure 4. The indentation depth and indentation strain rate point out that the creep strength in the DR is slightly higher than in the IR. To compare the determined values with macroscopic tensile creep experiments, the minimum strain rates are plotted in a Norton plot together with results from Wollgramm et al. [22], as shown in Figure 4(b). These results are also from alloy ERBO1, but in the fully heat-treated condition (ERBO1C). Therefore the γ′ volume fraction is higher, which explains the lower creep rates. It should also to be noted that ERBO1C exhibits a double creep minimum [22] similar to other Ni- and Co-base superalloys [23, 24]. The duration of the indentation creep experiments is rather short with 3 hours and comparable to the duration until the first creep minimum in the macroscopic creep experiments, which is reached after about 10 hours. Contrarily, the second creep minimum is reached after 100 hours or more. Therefore, the first creep minimum was selected for comparison with the macroscopic tensile creep experiments. The determined stress exponent of 4.7 from the indentation creep experiments is in very good agreement with the stress exponent of 5 from the macroscopic tensile creep experiments.

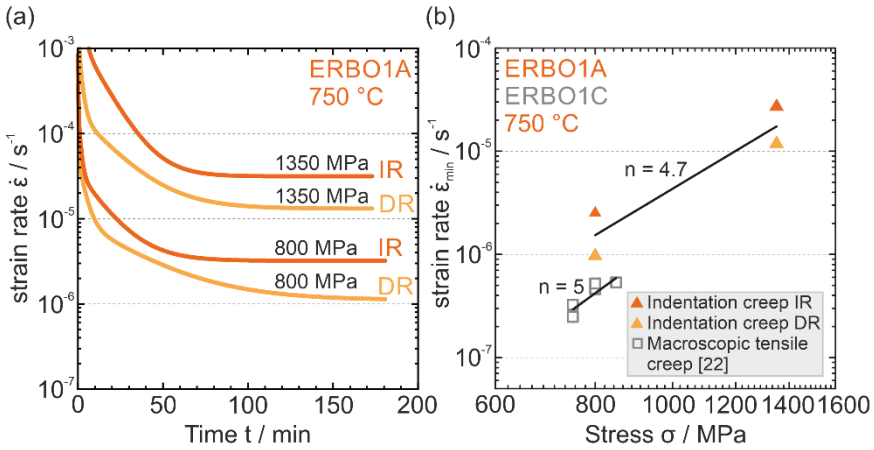

Figure 4: (a) Results from indentation creep tests in the DR and IR tested at 750 °C under 800 MPa and 1350 MPa. The creep data at 800 MPa corresponds to the indents shown in Figure 2. (b) Norton plot of the indentation creep experiments in comparison with macroscopic tensile creep experiments of the fully heat treated alloy ERBO1C [22].

The chemical composition measured via EDS at the locations of the indents sites (see Figure 3) are listed in Table 2. The solid fraction at the particular position can then be calculated from the measured concentrations of Re and Ta together with Figure 2(e). The results emphasize the difference in microstructure at varying positions. While the microstructure at the indentation site in the DR solidifies in the beginning, with a maximum solid fraction f_s of 21 %, the indentation site in the IR solidifies between 40 % to 80 % solid fraction.

Table 2: Concentration at the indentation sites in the DR and IR (see Figure 3) measured via EDS.

Region	Concentration / at. %								
	Co	Ni	Al	W	Ti	Ta	Cr	Re	Mo
DR	9.9	61.1	15.6	3.1	0.9	1.6	6.0	1.3	0.4
	±0.7	±2.4	±2.5	±0.2	±0.1	±0.5	±1.0	±0.3	±0.1
IR	9.3	60.9	14.8	2.6	1.2	2.3	7.3	1.0	0.6
	±0.3	±1.3	±0.8	±0.1	±0.0	±0.1	±1.1	±0.2	±0.0

Besides the indentation creep experiments, micropillar compression tests at selected positions were conducted. As shown in Figure 5, the micropillars were prepared in different regions of the microstructure and were subsequently tested at 785 °C. As of now, this is the highest temperature at which micropillar compression tests have been performed on superalloys.

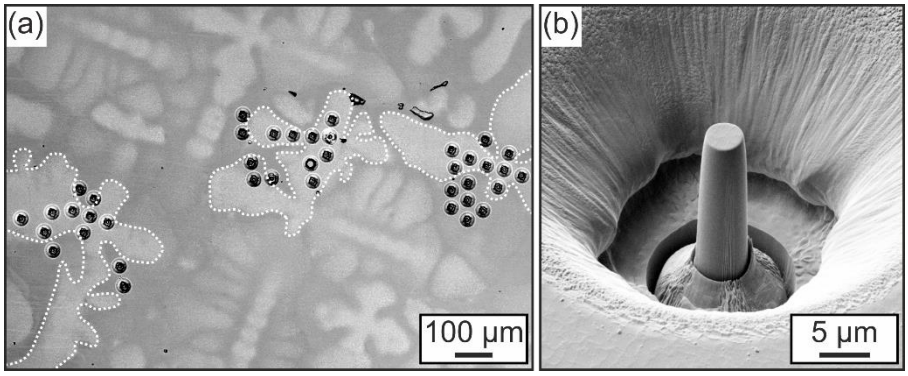

Figure 5: (a) Micropillar in the DR and IR of the alloy ERBO1A and (b) higher magnification of one of the freestanding micropillar.

No drift correction was conducted, since the thermal drift is very low with around 2 nm/min. Especially for the determination of the yield strength $R_{p0.2}$, which is reached within short experiment duration, the thermal drift should have a rather small influence on the measured data. The resulting stress strain diagrams are shown in Figure 6(a) and the determined yield strengths in Figure 6(b). The different regions - DR and IR - are separated by different colors. An evaluation of the yield strength $R_{p0.2}$ of pillars from the DR and IR results in an about 10 % higher strength in the DR. This is in good agreement with the slightly improved creep strength in the DR. It has to be noted that one micropillar in the IR shows a significantly lower strength compared to the others. The SEM image of this pillar shows an interface like contrast change at the bottom, which could indicate a sub-grain boundary. The strength level is in general comparable to literature data from CMSX-4 [6] and René N5 [25], albeit no direct comparison is possible due to different micropillar diameters, orientations and testing temperatures. Shade et al. [25] have also reported higher strengths in the DR measured on pillar diameters of 5 µm and <123> orientation at room temperature. A higher hardness in the DR is also reported in the literature [26, 27].

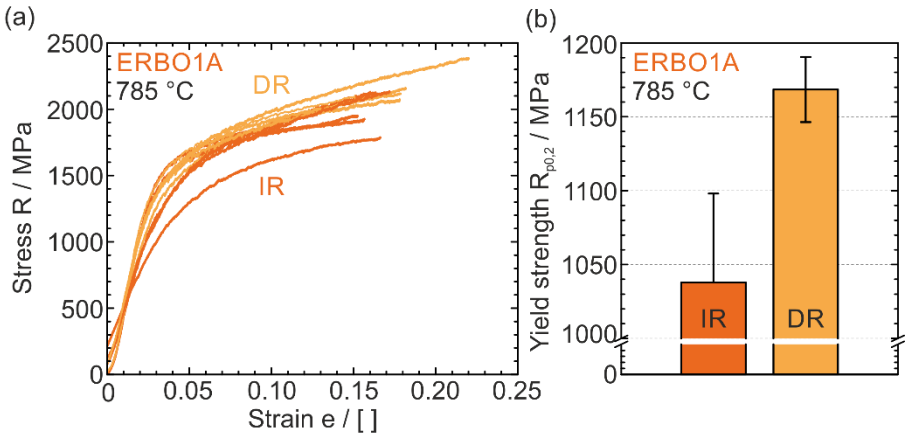

Figure 6: Results from micropillar compression testing in the DR and IR of the alloy ERBO1A at 785 °C, (a) stress-strain-curves and (b) yield strength $R_{p0.2}$.

3.3 Correlation of microstructure and local mechanical properties

For a detailed analysis of the increased strength in the DR, a local microstructure analysis was carried out at the indentation creep sites and the strength contribution from solid solution hardening and precipitation hardening was estimated.

The strength σ_{sum} of superalloys results mainly from the solid solution hardening in the γ phase σ_{MK} and the γ′ precipitation hardening σ_P:

$$\sigma_{sum} = \sigma_{MK} + \sigma_P \quad (1)$$

The increase of strength by solid solution hardening in Ni can be estimated after Gypen and Deruyttere [28] from the sum of the contributions of individual alloying elements:

$$\Delta\sigma_{MK} = \left(\sum_i K_i^{1/n} \cdot c_i^{\gamma}\right)^n \quad (2)$$

The solid solution hardening coefficient K_i describes the element specific contribution to the strength increase in dependence of the concentration c_i^{γ}. The Labusch model [29] suggests for the strengthening exponent *n* to be 2/3, which is used here.

For the estimation of the strength contribution from solid solution hardening in the γ phase in the DR and IR, the elements W, Re, Ta and Mo will be considered, since they contribute strongly to the solid solution hardening [30]. The solid solution hardening coefficients K_i of W, Re, Ta and Mo in Ni were calculated from data of [31, 32] to 1.5 GPa/at. $\%^{2/3}$, 1.5 GPa/at. $\%^{2/3}$, 1.8 GPa/at. $\%^{2/3}$ and 1.6 GPa/at. $\%^{2/3}$ respectively. The used data for the calculation was generated at 77 K and therefore the solid solution hardening coefficients at room temperature could be significantly lower. However, the calculated strengthening contributions are only estimations and the qualitative results should be equal at both temperatures.

The concentration of the alloying element in the γ phase c_i^{γ} was estimated with equation (3):

$$c_i^{\gamma} = \frac{c_i^{\gamma'}}{k_i^{\gamma'/\gamma}} \quad (3)$$

Whereas $c_i^{\gamma'}$ is the concentration of an element in the γ′ phase, and $k_i^{\gamma'/\gamma}$ is the partitioning coefficient between the γ and γ′ phase. The concentration in the γ′ phase $c_i^{\gamma'}$ was estimated by equation (4):

$$c_i^{\gamma'} = \frac{c_i \cdot k_{i,DR/IR}^{\gamma'/\gamma}}{\left[\left(1 - f_{V,DR/IR}\right) + f_{V,DR/IR} \cdot k_{i,DR/IR}^{\gamma'/\gamma}\right]} \quad (4)$$

The concentration c_i was taken from the determined chemical composition at the indentation sites (see Table 2) and the partitioning coefficients $k_{i,DR/IR}^{\gamma'/\gamma}$ were calculated for the DR and IR from the composition of the γ and γ′ phase determined by Parsa et al. [15] in the fully heat treated state. The γ′ volume fractions $f_{V,DR/IR}$ were directly determined at the indentation sites of the experiments at 750 °C under 800 MPa to a volume fraction of $f_{V,DR}$ = 58.0 ± 3.9 % in the DR and $f_{V,IR}$ = 62.3 ± 2.0 % in the IR. Since, the partitioning coefficients $k_i^{\gamma'/\gamma}$ are only slightly different in the DR and IR [15], it is assumed that they are equal to those of the as-cast state. Nevertheless, the calculated concentrations of the γ and γ′ phase in Table 3 are only an estimation.

Table 3: Concentration of the γ and γ′ phase estimated by equations (1) and (2) in at. %.

Region	Phase	Co	Ni	Al	W	Ti	Ta	Cr	Re	Mo
DR	γ	16.2	51.8	3.5	4.0	0.1	0.1	12.7	3.0	0.7
		±1.2	±2.0	±0.6	±0.3	±0.0	±0.0	±2.0	±0.6	±0.2
	γ′	5.4	67.9	24.4	2.4	1.5	2.6	1.3	0.1	0.2
		±0.4	±2.6	±3.9	±0.2	±0.2	±0.8	±0.2	±0.0	±0.1
IR	γ	16.0	50.8	3.7	3.5	0.1	0.1	16.3	2.4	1.0
		±0.5	±1.1	±0.2	±0.1	±0.0	±0.0	±2.4	±0.4	±0.1
	γ′	5.3	67.1	21.6	2.0	1.8	3.7	1.8	0.1	0.3
		±0.2	±1.4	±1.2	±0.0	±0.0	±0.2	±0.3	±0.0	±0.0

According to the model of Gypen and Deruyttere [28], together with the in Table 3 estimated concentrations for W, Re, Ta and Mo in the γ phase, solid solution hardening in the γ phase σ_{MK} is 276 MPa in the DR and 258 MPa in the IR. This increased strength by 18 MPa in the DR compared to the IR is mainly due to the higher content of the strong solid solution hardening elements W and Re in the γ phase of the DR.

The strength increase from the interaction of dislocations with γ′ precipitates σ_P is defined as followed:

$$\sigma_P = M \cdot \tau_P \tag{5}$$

Where τ_P is the critical resolved shear stress for precipitation hardening and M is the Taylor factor and has a value of 3 [33]. In order to estimate the γ′ precipitation hardening the unified approach of Galindo-Nava [34] for γ′ precipitate cutting is used for the critical resolved shear stress τ_P:

$$\tau_P = \frac{\gamma_{APB} \cdot l}{2b \cdot (\Lambda_1 + 2r)} \tag{6}$$

While γ_{APB} is the antiphase boundary energy, l is the segment length of the leading partial dislocation, b is the burgers vector, Λ_1 is the average precipitate distance along the dislocation line and r is the precipitate radius. Since the precipitate radius in the DR and IR is larger than the radius with the highest counteracting force r_m (see equation (7)), strong pair-coupling can be assumed.

$$r_m = \frac{G \cdot b^2}{2\gamma_{APB}} \tag{7}$$

In this case l is defined by (8) and Λ_1 by (9) with L as the effective precipitate distance (10).

$$l = 2(r^2 - (r - r_m)^2)^{1/2} \tag{8}$$

$$\Lambda_1 = L - l \tag{9}$$

$$L = \left(\frac{2\pi}{3f_V}\right)^{1/2} \tag{10}$$

The calculation refers to the cutting of edge dislocations within γ′ precipitates. Here it is worth to be mentioned that the model of Galindo-Nava et al. [34] is valid for spherical precipitates, while the precipitates in ERBO1A are more cubic. This could have a significant influence on the calculated strength contribution from precipitation hardening. The γ′ precipitate sizes in the

DR and IR were also directly determined at the indentation sites of the experiments at 750 °C under 800 MPa to 480 nm in the DR and 600 nm in the IR. An shear modulus *G* of 90.2 GPa at 1000 K was calculated after [35] with the elastic constants of ERBO1C [36] and a Burgers vector *b* of 0.254 nm, that was taken from [37] for the γ′ hardened Ni base Superalloy Nimonic PE16. Considering the different concentrations of elements in the γ′ phase in the DR and IR the antiphase boundary (APB) energy was estimated after the model of Crudden et al. [38]:

$$\gamma_{APB} = \gamma_{APB}^{0} + \sum_{i=1}^{n}\left(u_i \cdot c_i^{\gamma'}\right) \quad (11)$$

Whereas γ_{APB}^{0} describes the APB energy of Ni_3Al and is 195 ± 13 mJ/m^2. The model assumes a linear relationship between the contributions of the individual alloying elements *i*. The coefficient u_i describes the change of the APB energy by an element *i*, which has the concentration $c_i^{\gamma'}$ in the γ′ phase. The coefficients to describe the APB energy change u_i of Cr, Mo, W, Ta, and Ti were calculated to -1.7 mJ/m^2, -1.7 mJ/m^2, 4.6 mJ/m^2, 27.1 mJ/m^2 and -15 mJ/m^2, respectively [38]. The concentrations $c_i^{\gamma'}$ can be found in Table 3. This results in an APB energy γ_{APB} of 297 mJ/m^2 in the DR and 328 mJ/m^2 in the IR. It is unlikely that the alloying elements Co, Ni, Al and Re lead to a further increase of the APB energy in the IR, as Co, Ni and Re have a comparable concentration in the γ′ phase in the DR and IR.

Therefore, the calculated strength contribution by precipitation hardening σ_P in the DR is 297 MPa while it is 279 MPa in the IR. This reveals that the strength in the DR is 18 MPa higher than in the IR, despite the higher γ′ volume fraction and the higher APB energy in the IR due to the higher concentration of γ′ forming element Ta. The decisive factor is the smaller γ′ precipitate size in the DR (see Equation 6) which compensates the lower γ′ volume fraction and APB energy under the assumption of γ′ precipitate cutting by strong pair-coupling of the dislocations.

The theoretically calculated strength contributions result in a total strength of 573 MPa in the DR and 537 MPa in the IR. The 36 MPa higher strength of the DR supports the results of the indentation creep and micropillar compression tests, in which also slightly better mechanical properties in the DR could be determined.

Laplanche et al. [39] also investigated the DR and IR of the alloy ERBO1 but by an in-situ SEM micromechanical test technique at room temperature and in the fully heat treated condition ERBO1C. Contrary to the as-cast condition in this study, they observed a higher strength in the IR than in the DR. There the elemental distribution was more homogeneous in the heat treated condition, the γ′ volume fraction in the IR of 77 % and in the DR of 72 % was much higher, but the precipitate size with nearly equal values of 600 nm in the IR and 590 nm in the DR were much closer to each other. This might lead to a higher strength of the IR due to additional strength contributions of 5 % from the slightly higher γ′ volume fraction and 6 % from the narrower γ′ channels, as stated in [39].

Thus, for the fully heat-treated state, a smaller difference in the local mechanical properties can be expected, despite the still existing but lower segregations, especially of Re. Even a reversal of the strength ratio of DR and IR is possible, as shown by Laplanche et al. [39], depending on the local γ′ morphology and volume fraction.

4. Conclusions

The local microstructural and mechanical differences of the as-cast single crystalline Ni-base alloy ERBO1A were investigated by SEM, EDS and EPMA measurements and by indentation

creep and micropillar compression tests at elevated temperatures. Together with theoretical calculations on the local strength the following conclusions can be drawn:

- ERBO1 shows a distinct dendritic microstructure in the as-cast state and the solid solution hardening elements Re and W segregate in the dendritic region (DR), whereas the γ′ forming element Ta segregates in the interdendritic region (IR).

- The indentation creep experiments at 750 °C reveal a two times lower creep rate in the DR than the IR and the micropillar compression tests at 785 °C show an about 10 % higher yield strength in the DR than in the IR.

- The calculated strength increase by solid solution hardening is 276 MPa for the DR and 258 MPa for the IR due to higher concentrations of W and Re. The calculated strength increase by γ′ precipitation hardening is 297 MPa for the DR and 279 MPa for the IR. This is caused by a smaller γ′ precipitate size in the DR, despite a higher γ′ volume fraction and a higher APB energy in the IR due to an enrichment of Ta.

- The calculations are in good agreement with the nanomechanical measurements of a higher strength in the DR than in the IR of the as-cast condition. However, the differences might vanish or even invert in the fully heat treated condition, due to less segregation, higher γ′ volume fractions and a more similar γ′ size between dendrite core and interdendritic regions.

5. Acknowledgments

The authors gratefully acknowledge funding by the Deutsche Forschungsgemeinschaft (DFG) through projects A6 of the Collaborative Research Centre SFB/TR 103 “From Atoms to Turbine Blades – a Scientific Approach for Developing the Next Generation of Single Crystal Superalloys” and thank S. Giese and C. Schunk from the Institute I: General Materials Properties at FAU for their support for milling the micropillars. Furthermore, the authors thank Siwen Gao from the Interdisciplinary Centre for Advanced Materials Simulation of the Ruhr University Bochum for the FE simulation image.

6. References

1. Neumeier S, Pyczak F, Göken M (2011) Influence of rhenium and ruthenium on the local mechanical properties of the γ and γ' phases in nickel-base superalloys. Philos Mag 91:4187–4199. doi: 10.1080/14786435.2011.607139

2. Rehman H ur, Durst K, Neumeier S, Parsa AB, Kostka A, Eggeler G, Göken M (2015) Nanoindentation studies of the mechanical properties of the μ phase in a creep deformed Re containing nickel-based superalloy. Mater Sci Eng A 634:202–208. doi: 10.1016/j.msea.2015.03.045

3. Göken M, Kempf M (1999) Microstructural properties of superalloys investigated by nanoindentations in an atomic force microscope. Acta Mater 47:1043–1052. doi: 10.1016/S1359-6454(98)00377-2

4. Chu SNG, Li JCM (1977) Impression creep; a new creep test. J Mater Sci 12:2200–2208. doi: 10.1007/BF00552241

5. Trenkle JC, Packard CE, Schuh CA (2010) Hot nanoindentation in inert environments. Rev Sci Instrum 81:073901. doi: 10.1063/1.3436633

6. Korte S, Stearn RJ, Wheeler JM, Clegg WJ (2012) High temperature microcompression and nanoindentation in vacuum. J Mater Res 27:167–176. doi: 10.1557/jmr.2011.268

7. Dorner D, Röller K, Skrotzki B, Stöckhert B, Eggeler G (2003) Creep of a TiAl alloy: a comparison of indentation and tensile testing. Mater Sci Eng A 357:346–354. doi: 10.1016/S0921-5093(03)00205-3

8. Mathew MD, Naveena, Vijayanand D (2013) Impression Creep Behavior of 316LN Stainless Steel. J Mater Eng Perform 22:492–497. doi: 10.1007/s11665-012-0290-4

9. Sundar RS, Kutty TRG, Sastry DH (2000) Hot hardness and creep of Fe_3Al-based alloys. Intermetallics 8:427–437. doi: 10.1016/S0966-9795(99)00118-1

10. Cross GLW, O′Connell BS, Pethica JB, Rowland H, King WP (2008) Variable temperature thin film indentation with a flat punch. Rev Sci Instrum 79:013904. doi: 10.1063/1.2830028

11. Rowland HD, King WP, Cross GLW, Pethica JB (2008) Measuring Glassy and Viscoelastic Polymer Flow in Molecular-Scale Gaps Using a Flat Punch Mechanical Probe. ACS Nano 2:419–428. doi: 10.1021/nn700211g

12. Chu SNG, Li JCM (1979) Impression creep of β-tin single crystals. Mater Sci Eng 39:1–10. doi: 10.1016/0025-5416(79)90164-2

13. Durst K, Göken M (2004) Micromechanical characterisation of the influence of rhenium on the mechanical properties in nickel-base superalloys. Mater Sci Eng A 387–389:312–316. doi: 10.1016/j.msea.2004.03.079

14. Matschkal-Amberger D, Kolb M, Neumeier S, Gao S, Hartmaier A, Durst K, Göken M (2019) New flat-punch indentation creep testing approach for characterizing the local creep properties at high temperatures. Mater Des 183:108090. doi: 10.1016/j.matdes.2019.108090

15. Parsa AB, Wollgramm P, Buck H, Somsen C, Kostka A, Povstugar I, Choi P-P, Raabe D, Dlouhy A, Müller J, Spiecker E, Demtroder K, Schreuer J, Neuking K, Eggeler G (2015) Advanced Scale Bridging Microstructure Analysis of Single Crystal Ni-Base Superalloys: Advanced Scale Bridging Microstructure Analysis. Adv Eng Mater 17:216–230. doi: 10.1002/adem.201400136

16. Greer JR, De Hosson JThM (2011) Plasticity in small-sized metallic systems: Intrinsic versus extrinsic size effect. Prog Mater Sci 56:654–724. doi: 10.1016/j.pmatsci.2011.01.005

17. Conte M, Mohanty G, Schwiedrzik JJ, Wheeler JM, Bellaton B, Michler J, Randall NX (2019) Novel high temperature vacuum nanoindentation system with active surface referencing and non-contact heating for measurements up to 800 °C. Rev Sci Instrum 90:045105. doi: 10.1063/1.5029873

18. Wheeler JM, Brodard P, Michler J (2012) Elevated temperature, in situ indentation with calibrated contact temperatures. Philos Mag 92:3128–3141. doi: 10.1080/14786435.2012.674647

19. Koßmann J, Zenk CH, Lopez-Galilea I, Neumeier S, Kostka A, Huth S, Theisen W, Göken M, Drautz R, Hammerschmidt T (2015) Microsegregation and precipitates of an as-cast Co-based superalloy – microstructural characterization and phase stability modelling. J Mater Sci 50:6329–6338. doi: 10.1007/s10853-015-9177-8

20. Karunaratne MSA, Cox DC, Carter P, Reed RC (2000) Modelling of the Microsegregation in CMSX-4 Superalloy and its Homogenisation During Heat Treatment. In: Green K, Kissinger R, Pollock TM (eds) Superalloys 2000. The Minerals, Metals & Materials Society, Warrendale PA, pp 263–272

21. Ganesan M, Dye D, Lee PD (2005) A technique for characterizing microsegregation in multicomponent alloys and its application to single-crystal superalloy castings. Metall Mater Trans A 36:2191–2204. doi: 10.1007/s11661-005-0338-2

22. Wollgramm P, Bürger D, Parsa AB, Neuking K, Eggeler G (2016) The effect of stress, temperature and loading direction on the creep behaviour of Ni-base single crystal superalloy miniature tensile specimens. Mater High Temp 33:346–360. doi: 10.1080/09603409.2016.1186414

23. Xue F, Zenk CH, Freund LP, Hoelzel M, Neumeier S, Göken M (2018) Double minimum creep in the rafting regime of a single-crystal Co-base superalloy. Scr Mater 142:129–132. doi: 10.1016/j.scriptamat.2017.08.039

24. Wu X, Wollgramm P, Somsen C, Dlouhy A, Kostka A, Eggeler G (2016) Double minimum creep of single crystal Ni-base superalloys. Acta Mater 112:242–260. doi: 10.1016/j.actamat.2016.04.012

25. Shade PA, Uchic MD, Dimiduk DM, Viswanathan GB, Wheeler R, Fraser HL (2012) Size-affected single-slip behavior of René N5 microcrystals. Mater Sci Eng A 535:53–61. doi: 10.1016/j.msea.2011.12.041

26. Rehman H ur (2016) Solid Solution Strengthening and Difusion in Nickel- and Cobalt-based Superalloys. Ph.D. thesis, Friedrich-Alexander Universität Erlangen-Nürnberg

27. Tromas C, Arnoux M, Milhet X (2012) Hardness cartography to increase the nanoindentation resolution in heterogeneous materials: Application to a Ni-based single-crystal superalloy. Scr Mater 66:77–80. doi: 10.1016/j.scriptamat.2011.09.042

28. Gypen LA, Deruyttere A (1977) Multi-component solid solution hardening: Part 1 Proposed model. J Mater Sci 12:1028–1033. doi: 10.1007/BF00540987

29. Labusch R (1970) A Statistical Theory of Solid Solution Hardening. Phys Status Solidi B 41:659–669. doi: 10.1002/pssb.19700410221

30. Roth HA, Davis CL, Thomson RC (1997) Modeling solid solution strengthening in nickel alloys. Metall Mater Trans A 28:1329–1335. doi: 10.1007/s11661-997-0268-2

31. Mishima Y, Ochiai S, Hamao N, Yodogawa M, Suzuki T (1986) Solid Solution Hardening of Nickel – Role of Transition Metal and B-subgroup Solutes. Trans Jpn Inst Met 27:656–664. doi: 10.2320/matertrans1960.27.656

32. Diologent F, Caron P (2004) On the creep behavior at 1033 K of new generation single-crystal superalloys. Mater Sci Eng A 385:245–257. doi: 10.1016/S0921-5093(04)00925-6

33. Cottrell AH (1965) Dislocation and plastic flow in crystals. Clarendon Press, Oxford

34. Galindo-Nava EI, Connor LD, Rae CMF (2015) On the prediction of the yield stress of unimodal and multimodal γ′ Nickel-base superalloys. Acta Mater 98:377–390. doi: 10.1016/j.actamat.2015.07.048

35. Pottebohm H, Neite G, Nembach E (1983) Elastic properties (the stiffness constants, the shear modulus and the dislocation line energy and tension) of Ni-Al solid solutions and of the Nimonic alloy PE16. Mater Sci Eng 60:189–194. doi: 10.1016/0025-5416(83)90001-0

36. Demtröder K, Eggeler G, Schreuer J (2015) Influence of microstructure on macroscopic elastic properties and thermal expansion of nickel-base superalloys ERBO/1 and LEK94. Mater Sci Eng Technol 46:563–576. doi: 10.1002/mawe.201500406

37. Nembach E, Neite G (1985) Precipitation hardening of superalloys by ordered γ′-particles. Prog Mater Sci 29:177–319. doi: 10.1016/0079-6425(85)90001-5

38. Crudden DJ, Mottura A, Warnken N, Raeisinia B, Reed RC (2014) Modelling of the influence of alloy composition on flow stress in high-strength nickel-based superalloys. Acta Mater 75:356–370. doi: 10.1016/j.actamat.2014.04.075

39. Laplanche G, Wieczorek N, Fox F, Berglund S, Pfetzing-Micklich J, Kishida K, Inui H, Eggeler G (2018) On the influence of crystallography and dendritic microstructure on micro shear behavior of single crystal Ni-based superalloys. Acta Mater 160:173–184. doi: 10.1016/j.actamat.2018.08.052